Biophysical Journal Volume 106 May 2014 2233–2242

A Computational Model for the Loss of Neuronal Organization in Microcolumns

Maxwell Henderson, Brigita Urbanc, and Luis Cruz*
Department of Physics, Drexel University, Philadelphia, Pennsylvania

ABSTRACT A population of neurons in the cerebral cortex of humans and other mammals organize themselves into vertical microcolumns perpendicular to the pial surface. Anatomical changes to these microcolumns have been correlated with neurological diseases and normal aging; in particular, in area 46 of the rhesus monkey brain, the strength of microcolumns was shown to decrease with age. These changes can be caused by alterations in the spatial distribution of the neurons in microcolumns and/or neuronal loss. Using a three-dimensional computational model of neuronal arrangements derived from thin tissue sections and validated in brain tissue from rhesus monkeys, we show that neuronal loss is inconsistent with the findings in aged individuals. In contrast, a model of simple random neuronal displacements, constrained in magnitude by restorative harmonic forces, is consistent with observed changes and provides mechanistic insights into the age-induced loss of microcolumnar structure. Connection of the model to normal aging and disease are discussed.

INTRODUCTION

Neuronal structures in the brain exhibit different levels of organization that span a wide range of scales (1,2). At the macroscopic scale, neurons arrange themselves into layers; whereas at the smallest microscopic scale in some parts of the brain, neurons arrange into microcolumns. These microcolumns, also known as minicolumns, are micrometer-sized anatomical structures in the cerebral cortex that consist of neurons organized into vertical columns. These columns span, in many cases, from the subcortical white matter to the pial surface in the brains of humans and some primates (1–10), with similar structures also observed in dolphins and rats (10–13). Determining whether these microcolumns are functional units is still a matter of research. Some studies suggest that microcolumns are fundamental computational units of the brain (1–5,7,9,10), whereas others are more skeptical (14–21). Recent results, however, indicate that neurons within microcolumns are involved in the executive control of behavior in rhesus monkeys (22).

Independent of the anatomical function of microcolumns, changes in their structure have been widely characterized in the literature and may be predictors of or serve as proxy to underlying brain pathology. For example, studies have correlated changes in the microcolumnar structure to neurological diseases such as Alzheimer's disease (23,24), schizophrenia (25–29), Down syndrome (30), autism (31–40), and dyslexia (40,41). Even in normal aging, where cognitive decline is not accompanied by significant neuronal loss in the cerebral cortex (42–44), loss of microcolumnar strength in rhesus monkeys (45–48) and microcolumnar thinning in humans (49–51) was correlated to both age and cognitive decline that may be a consequence of the loss of other underlying structures (52).

The studies mentioned above offer a correlation between changes in microcolumnar characteristics and age or disease. However, the exact neurobiological mechanisms underlying this cognitive decline and neuropathology are not known. As a step toward unravelling these deleterious mechanisms, we need to understand what kinds of alterations in the arrangement of neurons within microcolumns are consistent with the observed quantitative changes. Specifically, it would be useful to know how neurons in normal aging rearrange as a function of time into structures with altered microcolumnar strengths and widths, as defined in Cruz et al. (45). Likewise, it would be important to know if the finite, but nonsignificant, loss of neurons during the aging process (<10% (42,44,53)) plays a role in these observed changes as a uniform loss across brain regions or as local losses within micron-sized clusters of neurons. Finally, understanding how different types of neuronal perturbations affect measures of microcolumnarity could give credence to different models of aging. For instance, plausible mechanisms for the observed changes in microcolumns could be that neurons experience alterations in their apical dendrites or axons along microcolumns, in their basal dendrites, or more generally on the entire support matrix keeping neurons in place. This assumption has a biophysical basis, as it is suspected that the extracellular matrix in the brain provides a degree of neuroprotection (54–57). These insights could potentially give clues to changes in other types of cells surrounding neuronal microcolumns, such as dendrites, glia, and oligodendrocytes, among others.

Here, we introduce computational models to examine several mechanisms for neuronal positional disruption or deletions and test whether they are consistent with age-induced changes in microcolumnar organization.

Submitted October 22, 2013, and accepted for publication April 4, 2014.
*Correspondence: ccruz@drexel.edu
Editor: Richard Bertram.

0006-3495/14/05/2233/10 $2.00
http://dx.doi.org/10.1016/j.bpj.2014.04.012

Connection between different mechanisms of disruption and experimental observations are presented and their possible relevance to aging and neurological diseases is discussed.

METHODS

The computational models presented here apply specific transformations to three-dimensional (3D) ensembles of neurons corresponding to healthy individuals (48). These initial ensembles were generated using a previously developed computational methodology in which data from digital images of brain tissue were used to build a plausible 3D arrangement of neurons with statistical properties consistent with experimental data (48). Specifically, that previous methodology used measures of microcolumnarity (45) of a given tissue section to construct, using a density map calculation, the 3D representation of neurons with the same statistical properties observed in the experimental tissue. Once generated, these initial ensembles are used here as the starting point of stochastic simulations that test different models of displacement and deletion. For simplicity of calculation, the models presented here consider ensembles of neurons embedded in a Cartesian coordinate system (48). This restriction does not limit the scope of our work or our conclusions as we compare the results from our models with data obtained from straight sections of tissue that locally conform to this coordinate system (23,45–47). This approach is common and has been applied by others to avoid confounding effects from curved regions (23,28,30,49). However, the general nature of the methodology presented here allows for straightforward generalizations to other coordinate systems that could better describe curved regions of the brain such as those found in the lip or fundus of any sulcus.

Because neuronal microcolumns are uniquely defined by spatial locations of neurons, the models presented here only consider the (x,y,z) positions of neuronal bodies and alter these locations by specific processes. We consider two distinct models of disruption: deletion of neurons and iterative displacements of neurons from their original positions. In the deletion model, two mechanisms are tested. In the first mechanism, individual neurons are randomly deleted, and in the second, neurons within micrometer-sized groups or clusters are deleted. The deletion model is motivated by the small, but nonsignificant, neuronal loss in aging (42,44,53) and the more radical loss in neurological and neuropathological diseases (29,58–60). In the displacement model, neurons are iteratively displaced through three biologically motivated mechanisms: 1), isotropic, where the supporting matrix of neurons is compromised; 2), in the plane perpendicular to the microcolumnar axis (e.g., by possible atrophy to basal dendrites); and 3), along the microcolumnar axis (e.g., by possible atrophy to apical dendrites and/or axons), as proposed elsewhere (45,46). These displacements, on the order of one neuronal diameter (~5 μm), can give rise to the age-induced microcolumnar disruptions seen in Cruz et al. (46).

To determine which mechanism is applicable to aging, we compare microcolumnar properties between experiment and simulations. These microcolumnar properties are expressed in terms of measures of microcolumnarity, as previously formulated (45). Specifically, measures of microcolumnarity are derived from density maps generated from neuronal ensembles according to the procedure explained and summarized below (see Analyzing phase) (48). The measures of microcolumnarity are 1), S, the strength of microcolumns (ratio of the neuronal density within a microcolumn to the average neuronal density); 2), T, the strength of nearest-neighbor microcolumns (ratio of the neuronal density of the neighboring two microcolumns to the average neuronal density; also measures the degree of microcolumnar periodicity); 3), W, the microcolumnar width; 4), P, the distance between microcolumns; 5), L, the effective length (vertical span) of microcolumns; 6), and Y, the distance between neurons within a microcolumn (perpendicular to pia and parallel to microcolumns) (45). For convenience, we redefine the microcolumnar strength, S, in terms of F, defined by

$$F = (S - 1) \times 100. \quad (1)$$

In contrast to S, the new quantity F has a simpler interpretation, with its values ranging from $F = 0$ (no microcolumnarity) to $F > 0$ (microcolumnarity), and its units of excess percentage of neuronal density within the microcolumns relative to the global neuronal density.

Overview

There are three parts to our simulation methodology. The first part is the generating phase, in which, following our previous protocol (48), 3D neuronal arrangements are initially created to correspond to young individuals. Next is the simulation phase, where the initial neuronal positions are iteratively altered or deleted according to well-defined rules (schematically shown in Fig. 1 and discussed below). In the final, analyzing phase, two-dimensional (2D) thin sections are extracted from the larger 3D systems and their measures of microcolumnarity are obtained and compared with target experimental measures (from aged individuals). The target measures serve two purposes: 1), they ensure that the simulation phase follows a plausible model (if the target values could not be reached following the simulation rules, the rules are discarded), and 2), they set a maximum number of time steps over which the simulation is carried out.

As discussed above, two plausible models for the simulation phase are tested (see Fig. 1). These models are 1), random deletion of neurons, and 2), random displacements, in which neurons perform 3D unrestricted and restricted (by a linear restoring force) random walks. The first model considers neuron deletions, a mechanism that is nonsignificant in aging but evident in many neurodegenerative diseases. The second model is based on the hypothesis that the supporting matrix, which is formed from various cells and biological components that hold neurons in place, loses integrity and allows neurons to be displaced from their initial positions. In the unrestricted displacement mechanism, it is assumed that the supporting matrix does not pose any restrictions in displacement, whereas in the restricted displacement mechanism, the supporting matrix, although compromised, still poses restrictions on how far neurons can be displaced. All of these steps are discussed in detail below.

Generating phase

The method for generating a 3D neuronal ensemble corresponding to a young brain has been described in detail elsewhere (48). Briefly, a 3D neuronal block of size $484 \times 484 \times 484$ μm^3 (~0.11 mm^3) is created by first generating a crystalline arrangement of neurons. In this arrangement, neurons are placed in microcolumns a distance d away from each other. The bases on which the microcolumns are constructed are initially placed on

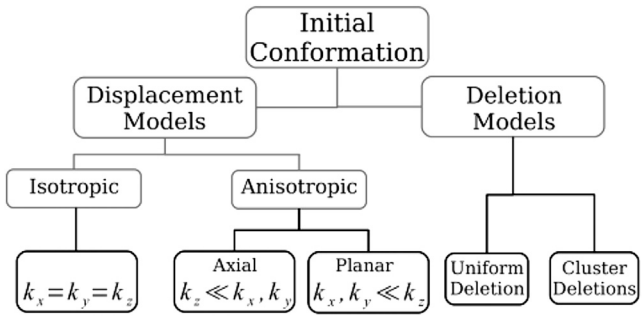

FIGURE 1 Schematic diagram of the different models and their mechanisms for neuronal displacement and deletion. The bottom row of the diagram represents the specific mechanisms of the respective models. The unrestricted displacement model is not shown.

the vertices of a hexagonal lattice. Using parameters consistent with experimental results from rhesus monkeys, a block would typically consist of a total of over 5000 neurons forming ~340 microcolumns. Although neurons in the brain are of various sizes, for simplicity of calculation all neurons are considered here as identically sized particles. The neuronal arrangements are then perturbed through a series of steps (parameterized by experimental measurement) to obtain a statistical correspondence between the generated block of 3D neurons and experimental tissue samples.

Specifically, a small percentage of neurons are first added at random positions (not belonging to the crystal arrangement) throughout the system of initial neurons. Because this insertion of randomly placed neurons increases the global density of the system, in the second step, the density is reduced to correspond to that experimentally observed by uniformly discarding initial and randomly placed neurons alike. In the third step, the positions of the microcolumns are randomly displaced (the bases of the columns are displaced in the plane perpendicular to them). Finally, individual neurons are displaced along the axis of the microcolumns and in the plane perpendicular to the microcolumns. In sum, this method systematically transforms a 3D crystalline lattice into a 3D spatial configuration of neurons that is characterized by microcolumnar measures consistent with those calculated from thin tissue sections (48). An example of such a computer-generated thin tissue slice is shown in Fig. 2 *A*. The example shown represents a thin slice from a young, healthy brain with well-defined microcolumns that can be observed in Fig. 2 *B*.

Simulation phase

Once the generating phase is completed, the different algorithmic models of displacement or neuronal deletion are implemented (Fig. 1).

The neuronal deletion model deletes a set of neurons from the initial neuronal ensembles. Two mechanisms of neuronal deletion, uniform and cluster deletions, are considered here. In the uniform-deletion mechanism, given a global deletion fraction, p (where the percentage of neuronal loss is $p \times 100$), for each neuron a random number q between 0 and 1 is generated and the neuron is deleted if $q < p$. Fig. 2 *D* shows one realization of this uniform deletion mechanism using the neuronal ensemble from Fig. 2 *A* as input. In the cluster deletion mechanism, too, each neuron is deleted if $q < p$, but in addition, all neurons within a radius R_{cl} from the deleted neuron are also deleted. Because neurons are deleted in clusters, the probability p does not represent the total neuronal loss. A new neuronal loss probability, p', is calculated by counting the remaining neurons, subtracting from the total initial number of neurons, and dividing the result by the total initial number of neurons. Fig. 2, *E* and *F*, shows two different examples of the cluster deletion mechanism with the smallest and biggest cluster sizes explored in our computational experiments. Both mechanisms result in the comparable neuronal losses of 20% and 18%, respectively.

In the unrestricted displacement model, neurons are iteratively displaced along 3D random walks that allow the neurons to eventually explore the totality of the available space. This model extends a previously developed 2D model to a 3D model (45,46). In the restricted displacement model, neurons also perform 3D random walks, but in addition, they are subjected to restorative harmonic forces. An example is shown in Fig. 2 *C*, where neurons performed a random walk under the constraints of a harmonic force. The restricted displacement model is based on the assumption that the positions of neurons embedded in support matrices with intact elasticity properties (young individuals) would, on average, be less perturbed than those in compromised mediums (aged individuals). Thus, we use strong restorative forces to simulate young brains with intact support matrices and weak restorative forces to model the compromised support matrices of aged brains. In accordance with this reasoning, and as a first approximation, we then consider age to be inversely proportional to the strength of the restorative force. To account for the fact that most neurons in the brain are not spherically symmetric (e.g., soma of pyramidal neurons have one axon process, one apical dendrite, and basal dendrites; thus, restorative forces may not be isotropic), the restricted displacement model is implemented by one of three mechanisms, the isotropic restorative force mechanism (3D - restoring equivalent harmonic forces in all directions), and two anisotropic restorative force mechanisms, explained in detail below.

The implementation of the 3D random walk is carried out by generating N randomly oriented vectors s_n ($n \in [1,N]$) of unit length for each neuron in the system. By assigning one vector of unit length per neuron, each neuron is then displaced in the direction of its vector by a distance on the order of ~0.7 μm. The process is then repeated. Because neurons are not allowed to overlap (volume exclusion), at the end of each displacement step, all neurons are tested for possible overlap with neighboring neurons (neuron diameter is taken as 10 μm) by calculating all pairwise distances and verifying that they are greater than one neuronal diameter. For neuron pairs (n,m) that are found to overlap, repulsive forces (of magnitude 1) are instead calculated for each neuron in the direction along the axis joining the neuron centers, where these forces (f_n,f_m) satisfy $f_m = -f_n$. Thus, a neuron n is displaced by either s_n (no overlap, random direction) or f_n (overlap along the separation axis).

For the restricted-displacement model, restorative harmonic force vectors, F_n, are added to either the random walk or nonoverlapping force vectors as appropriate, by calculating

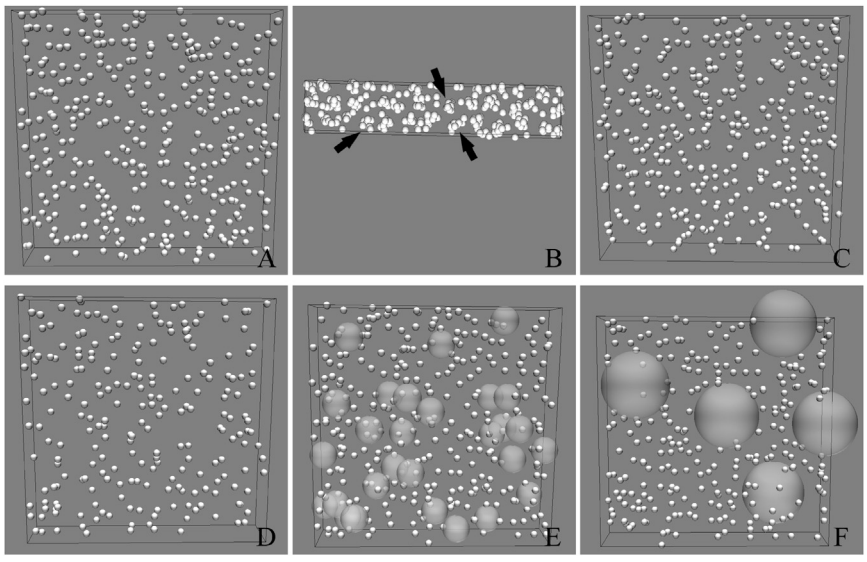

FIGURE 2 Typical 3D representations of neuronal ensembles resulting from the different displacement and deletion mechanisms. For clarity, the neurons, represented by bright small spheres, are those within a thin section obtained from the middle region of a larger cubic ensemble box. (*A*) Neuronal positions correspond to the original unaltered ensemble (healthy brains). (*B*) The same configuration as seen from the top, with arrows indicating representative microcolumns (microcolumns oriented along the axis coming out of the page). (*C*) A typical neuronal ensemble resulting from the harmonic force displacement mechanism using the smallest force constant ($k = 0.005$). (*D–F*) The neuronal-deletion mechanisms acting on the original ensemble from *A*, with uniform deletions corresponding to a maximum of ~35% neuronal loss (*D*), and deletions of clusters of radius 20 μm (*E*) and 50 μm (*F*) corresponding to neuronal losses of ~20% and ~18%, respectively.

$$F_{n,j} = -k_j\left(r_{n,j} - r^0_{n,j}\right), \quad (2)$$

where $F_{n,j}$ is the component of the restoring force along the j direction ($j = x,y,z$) acting on neuron n ($n = 1,\ldots,N$), k_j is the spring force constant (with Cartesian components k_x, k_y, and k_z), $r_{n,j}$ is the jth component of the current position vector of neuron n, and $r^0_{n,j}$ is the initial position vector of the neuron at time $t = 0$. For the values of k_j used here and the typical distances $r_{n,j} - r^0_{n,j}$, the range of values of $F_{n,j}$ are typically of the same order as those for the random walk and repulsive forces. To avoid large nonbiological displacements, the total displacement vector, proportional to the resultant force ($s_n + F_n$, no overlap; $f_n + F_n$, overlap), is further normalized to unity. This normalization is justified by considering that the hypothesized displacements of neurons are small due to an overdamped environment provided by the dense structure of the support matrix surrounding neurons. Fig. 2 *C* shows a thin section from one realization of the restricted displacement model where the final measures of microcolumnarity correspond to those in an aged individual. On visually comparing Fig. 2, *A–C*, it is not apparent that these two realizations are different. Differences only appear when considering many such realizations and calculating the measures of microcolumnarity over the entire ensemble of realizations.

Anisotropic restoring forces are now easily considered by implementing different values for k_x, k_y, and k_z. Thus, for modeling displacements preferentially along the z axis (the axis of the microcolumns) that result from hypothesized disruptions of the apical dendrite and/or axons, we use $k_x = k_y \gg k_z$. For modeling displacements on the xy plane (the plane perpendicular to the microcolumns) that result from hypothesized disruptions to basal dendrites, we use $k_z \gg k_x = k_y$. Finally, for modeling isotropic displacements (modeling uniform disruption to all supporting mechanisms of neurons) we use $k_x = k_y = k_z$.

Analyzing phase

After implementing the generation and simulation steps described above, the ensembles of neurons result in 3D coordinates describing microcolumnar structures at different stages of disruption. To make a comparison between experimental results and different simulation models, the cubic blocks of neuronal ensembles resulting from the generation and simulation steps are sliced at random angles to obtain quasi-2D 30-μm-thick sections (slabs) similar to experimentally prepared tissue samples (48). Neuron coordinates are then transformed into a new coordinate system (x',y',z'), where the z' direction is perpendicular to the plane of the slab. The random angles at which the 3D ensembles are cut provide slabs with varying lengths of microcolumn, as smaller angles would tend to cut parallel to the axis of microcolumns, whereas angles close to 90° would provide tangential cuts. Angles of cut are only considered in the 0–60° range to simulate plausible experimental slicing angles. The quasi-2D slabs are then converted into 2D systems reminiscent of experimental micrographs by collapsing the perpendicular axis of the sample ($z' = 0$), thus identifying each neuron by (x', y') coordinates only. These 2D neuronal positions are then analyzed using our density-map method to provide measures of microcolumnarity presented above and derived in Cruz et al. (45) (Fig. S1 in the Supporting Material shows the locations and regions in the density map that define these measures of microcolumnarity).

To characterize the degree of neuronal displacement, the average displacements of the neurons (with respect to their initial positions as a function of simulation time t) are obtained for neuron i by calculating the vector defined by the original position, $\overline{r_i}(0)$, and the position at time t, $\overline{r_i}(t)$, as

$$\overline{r_i}(0|t) = \overline{r_i}(t) - \overline{r_i}(0). \quad (3)$$

The average displacement of neurons (ensemble average) at time t is then obtained by calculating

$$R = \sqrt{\frac{\sum_i \overline{r_i}(0|t) \bullet \overline{r_i}(0|t)}{N}}, \quad (4)$$

where N is the total number of neurons in the system.

Statistics

To obtain adequate statistics for the restricted-displacement model, neurons are displaced for a total of 400 time steps. This maximum number of steps ensures convergence and stability of our results (for details, see Appendix A in the Supporting Material). After this number of steps, the restricted displacement model typically achieves a steady state in which statistical quantities fluctuate around equilibrium values (see below). Restorative forces are explored using eight different spring constant values for each of the 1D, 2D, and 3D mechanisms, ranging from 0.005 to 0.2. For each mechanism and spring constant value we generated 50 sets of 500 ensembles each. Because of the nature of our calculations, our method yields only statistical averages from a large number of generated neuronal ensembles. As such, individual ensembles of neurons do not correspond to particular experimental measurements; rather, the averages over populations are in agreement with experimental data. For the neuronal-deletion model, we examined several different percentages of neuronal loss from 0 to ~35% for both the uniform- and cluster-deletion mechanisms. Within the cluster-deletion mechanism, we studied three cluster sizes consisting of spheres 20, 33.3, and 50 μm in radius. In a similar way, for each percentage of neuronal loss and cluster size, we generated 50 sets of 500 ensembles each. Microcolumnar properties were calculated for each of these sets of neuronal ensembles and averaged over all ensembles. The statistical significance of each measure was assessed by calculating the standard error of the mean values.

RESULTS

In the next sections, we analyze and compare results from the neuronal-deletion model and the unrestricted- and restricted-displacement models. The comparisons are based on the microcolumnar properties resulting from each model and are made between the different models, as well as between the models and experimental results. Although the main microcolumnar property used in the comparisons is the percentage microcolumnar strength, F, all properties are presented and used in discerning the applicability of each model to aging.

Neuronal-deletion model

The simplest model of neuronal disruptions is considered in the uniform-deletion mechanism of the neuronal-deletion model. Fig. 3 *A* shows F versus the percentage of neural loss for this mechanism. The results indicate that F is not significantly affected up to a total neural loss of 35%. This is understood by considering that as neurons are progressively lost (higher values on the x axis), both microcolumnar and global densities decrease at the same rate, preserving the value of their ratio and, by definition, F. The situation is different for the cluster-deletion mechanism, in which neurons inside a sphere of a given radius are deleted. This

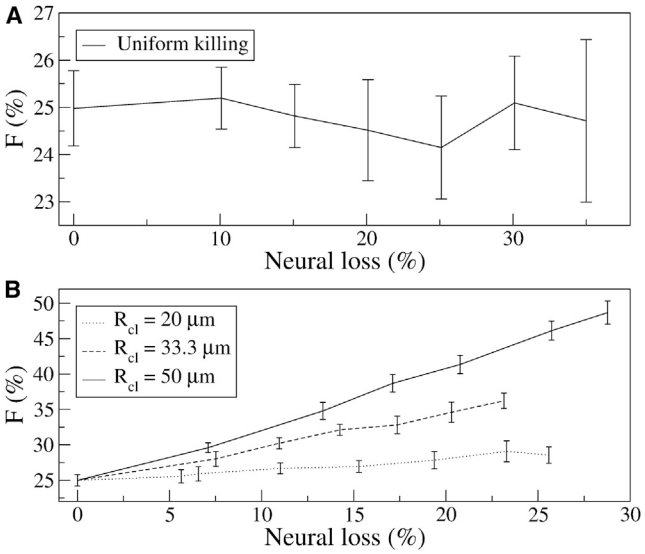

FIGURE 3 Percentage strength of microcolumns for the neuronal deletion mechanisms. (*A*) *F* is shown as a function of the percentage of neuronal loss where individual neurons were deleted at random. (*B*) *F* is shown as a function of total neuronal loss for the cases of neuronal cluster deletions within a sphere of radius R_{cl}.

mechanism seems more plausible in light of recent evidence suggesting that certain neurons are prone to loss in dementia and are concentrated in clusters within microcolumns (61). We were surprised to find that in this case, *F* increases with increasing neuronal loss (Fig. 3 *B*). This trend in *F* can be simply understood by considering that the density of neurons within microcolumns decreases at a slower rate (Fig. S2) compared to the global neuronal density (Fig. S3 *A*), resulting in an increase in the ratio between these two quantities and thus an increase in *F* as a function of neuronal loss. Also, because the rate of decrease of the density of neurons within microcolumns is slower for larger cluster deletions than for smaller clusters, *F* for the larger clusters will increase more steeply with increasing neuronal loss (Fig. 3 *B*). From a more mechanistic point of view, for the same neuronal loss, there is a larger number of smaller deletion clusters than of larger deletion clusters (Fig. 2, *E* and *F*). This means that the larger number of small deletion clusters more frequently affects the internal structure of microcolumns than the few larger clusters big enough to potentially eliminate entire microcolumns while leaving the vast majority of neurons relatively intact.

The other microcolumnar properties for the uniform- and cluster-deletion mechanisms are shown in Figs. S3 and S4, respectively. As with *F*, the microcolumnar properties for the case of uniform deletions did not show significant changes as a function of neuronal loss (Fig. S3). This again results from the fact that deleting neurons at random does not affect the microcolumnar measures (or, of more importance, their density maps (Fig. S5)), except by increasing the error bars for each quantity. Cluster deletions (Fig. S4), in contrast, introduce significant changes to *W*, *T*, and *L* as a function of neuronal loss. The increase in *T* (Fig. S4 *C*) is explained by the same mechanism that increases *F*, as *T* is also a ratio of local to global neuronal density. For *W* and *L*, the explanations are not apparent from an inspection of their corresponding density maps (Fig. S6). Some understanding can be achieved by examining the density profiles in the horizontal and vertical directions (along the lines in Fig. S7), as shown in Fig. S8. In Fig. S8 *A*, the trends in the width of the central peak show that the larger cluster sizes correlate with larger *W* values (resulting in Fig. S4 *B*). In a similar way, Fig. S8 *B* shows that exponential fits using the first two peaks would have a faster exponential decay for the two larger cluster-deletion cases than for the smallest cluster deletion (the relative heights of the peaks is larger for the larger deletion clusters), thus yielding a shorter length, *L*.

When comparing the measures of microcolumnarity presented above to experimental results, we observe that if neuronal loss results from normal aging, this loss as represented by the neuronal-deletion model is not responsible for the observed decrease of microcolumnar strength as a function of age. In other words, neuronal loss of the magnitude found in experiments (~10% (42,44,53)) and in our model (up to 35%) does not correlate with either the measures of microcolumnarity or the degree of cognitive impairment.

Neuron-displacement model

In search of a better model, we now consider the neuronal-displacement model. Its simplest implementation is the isotropic nonrestricted-displacement mechanism, where neurons are subjected to random-walk displacements isotropically, without restrictions. The average root mean-squared displacement, *R*, for this mechanism is the expected square-root time dependence, $R \sim t^{1/2}$ (Fig. S9 *A* and Appendix A in the Supporting Material). This behavioral trend is also observed when neurons are considered as nonoverlapping objects (Fig. S9 *A*), although in this case, the exponent in time is slightly smaller than 1/2. The similarity between these two exponents indicates that although neurons now experience collisions with each other as they diffuse away from their original positions, the collisions do not dominate the dynamics, which is consistent with the relatively large separation between neurons relative to their size (a dilute system). Histograms of $R(t)$ values for individual neurons at different time intervals also illustrate that in addition to following a Poisson distribution, the average neuronal displacement would always increase with time (Fig. S9 *B*). Thus, because neurons in a mature brain do not undergo large displacements relative to their linear size, a viable displacement model must introduce a constraint on the maximum displacement.

To this end, a modified model of random neuronal displacements considers neurons as random walkers under

the influence of a harmonic restoring force (see Methods). In Fig. 4 *A*, we show the time evolution of R for various values of the restoring-force constant ($k = 0.005$, 0.01, and 0.1) in the 3D isotropically restrained mechanisms, as compared to the unrestrained mechanism ($k = 0$). The results show that independent of the value of the spring constant, k, the long-time value of R reached a maximum value (i.e., $<R>_{max}$). In addition, the graph shows that this final value, $<R>_{max}$, is in general achieved after only a few hundred simulation steps. Histograms of R as a function of k for individual neurons are shown in Fig. 4 *B*, where for all nonzero values of k, the histograms converged to a stable (equilibrium) functional form. The values of $<R>_{max}$ not only were a function of k, but were different for each of the displacement mechanisms. Fig. 4 *C* compares the experimental and theoretical values of $<R>_{max}$ for each displacement mechanism. The theoretical values were determined by treating each neuron as a particle undergoing Brownian motion with harmonic constraints that prescribes $<R>_{max}$ as a power law of $1/k$ (see Eq. A16 in Appendix A of the Supporting Material).

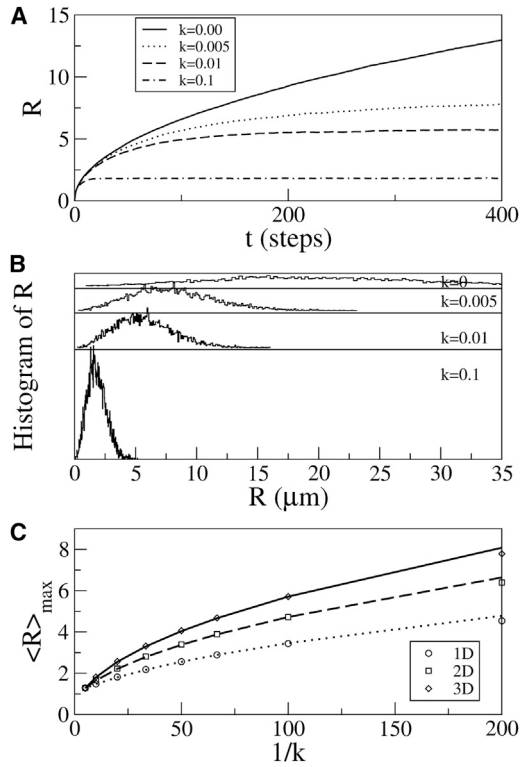

FIGURE 4 (*A*) $R(t)$ for one realization of a neuronal system undergoing random displacements (symmetric in all axes) with a harmonic restorative force for a selection of spring constant values. Systems with no restorative force ($k = 0$) exhibited an R value that increased without bounds. At equilibrium, R for systems with nonzero values of k reached a maximum average, $<R>_{max}$. See the Supporting Material for details of how to determine the critical number of time steps needed for convergence. (*B*) Histograms of R from individual neurons of the realizations shown in *A*, where the histogram for the spring constant value of $k = 0$ was calculated at $t = 1000$ and those for values of $k > 0$ at the equilibrium, $<R>_{max}$. (*C*) $<R>_{max}$ as a function of $1/k$ (*symbols*, taken from simulations) and k_x, k_y, and k_z (*solid lines*, from Eq. A16 in the Supporting Material).

From this figure, we can see that $<R>_{max}$ (for small k) is slightly lower than the theoretical predictions, probably due to particle collisions, a finding consistent with the results shown in Fig. S9 *A*.

In Fig. 5, *A* and *B*, we show F as a function of $1/k$ (*A*) and $<R>_{max}$ (*B*). Our data show that for the 1D displacement mechanism, compared to either the 2D or 3D displacement mechanisms, F decreased considerably more slowly with both $1/k$ and $<R>_{max}$. These results are reasonable, because displacements in the 1D model were predominantly along the axis of the microcolumns and thus preserved the number and density of neurons within the microcolumns. However, there is a small linear decrease in F due to the excluded-volume effect of neurons along the axis of the microcolumn, where some neurons are pushed out of the microcolumns. In contrast to the 1D mechanism, the 2D and 3D displacement mechanisms result in a decrease in F as a function of $1/k$ (Fig. 5 *A*). However, for the range of experimentally observed S ($1.25 \geq S \geq 1.17$, corresponding to $25 \geq F \geq 17$), both experiment and the model presented here can be approximated by a linear decrease in S and F (47). The sharper decrease in F as a function of $1/k$ in the 3D model compared to the 2D model is due to the increased number of degrees of freedom, which allows neurons to exit microcolumns in more directions and results in larger average displacements than in the 2D case (seen in Fig. 4 *C*).

Fig. 5 *B* shows F versus $<R>_{max}$ and demonstrates that for moderately larger values of $<R>_{max}$, F and $<R>_{max}$

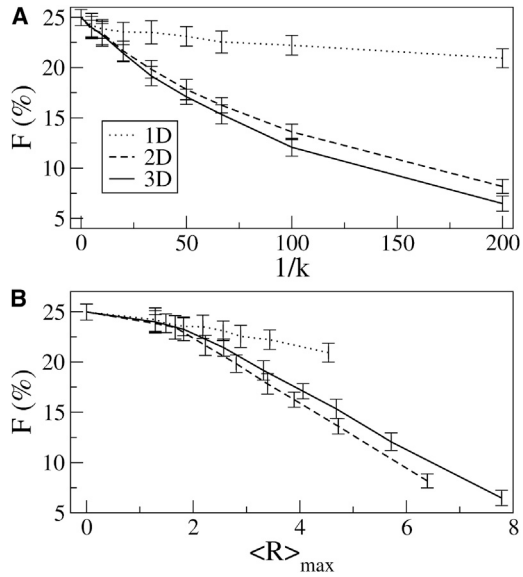

FIGURE 5 Percentage strength of microcolumns, F, for the harmonic force displacement mechanisms. (*A*) Percentage strength of microcolumns as a function of $1/k$ for different neuronal displacement mechanisms. (*B*) Percentage strength of microcolumns as a function of $<R>_{max}$ for different neuronal displacement mechanisms.

are linearly correlated. The rate of decrease of F in this graph is slower than for the previously reported 2D unrestricted model (46). Consequently, to model the same age-induced decrease in S (in the rhesus monkey brain), the average displacement would have to be $R \sim 4$ μm, a value slightly higher than that reported previously (46) but still of the same order as the size of a neuronal body. An additional feature of Fig. 5 *B* is that for the same value of $<R>_{max}$, the value of F for the 2D model is smaller than that for the 3D model. Because 2D displacements occur on the plane perpendicular to the microcolumns, they are more efficient in weakening microcolumnar strength than are 3D displacements.

Fig. 6 presents the other microcolumnar properties for the three displacement mechanisms. Although these plots show that the neuronal density (ρ), interneuron distance (Y), and intercolumn distance (P) do not significantly change as a function of $1/k$ (or of $<R>_{max}$, see Fig. S10), the width (W), strength of periodicity (T), and length (L) of microcolumns are affected. In the 1D case, values of the width decrease with $1/k$ (thinner microcolumns), whereas in the 2D case, they increase. These results can be understood by considering that in the 1D case, neurons are forced to stay within the axis of the microcolumn, and displacements thus result in a spread of neurons along the axis and a thinning of microcolumns. In the 2D case, displacements are essentially allowed only in the perpendicular plane, thus increasing microcolumnar widths. This result can also be understood by directly examining density maps that show thinner and wider microcolumns for the 1D and 2D cases, respectively (Fig. S11). A closer look at these density maps, focusing on the horizontal direction in the neuronal density profiles (neuronal density between horizontal lines c and d in Fig. S7) tells us that the width in the 1D case is significantly narrower and that in the 2D case significantly wider than the width in the 3D case (Fig. S12 *A*). These results are consistent with each model, where in the 2D case, widths increase because neurons are displaced in the direction perpendicular to the microcolumnar axis, whereas in the 1D case, widths decrease due to dispersion of neurons along the microcolumn.

The observed decay in the length of microcolumns in Fig. 6 for the 1D and 3D models can be equally well understood by examining the density maps in the vertical directions (that is, between vertical lines a and b in Fig. S7). It can be seen from the neuronal density profiles (Fig. S12 *B*) that the 1D and 3D cases had a faster decay (thus, shorter L) than the 2D case. Finally, the reduction in the microcolumnar periodicity (Fig. 6 *C*) for the 2D and 3D cases can be understood in terms of displacements of neurons away from the axis of the microcolumn that tended to reduce the microcolumnar density and thus the density of neurons in neighboring columns (i.e., the value of T).

DISCUSSION

Specific regions of the cerebral cortex in humans, primates, cats, rats, and some other animals are characterized by arrangements of neurons in microcolumns (1–13). It has been shown that this microcolumnar organization is affected by normal aging or cognitive decline (45–51), as well as by neurological disorders such as Alzheimer's disease (23–41).

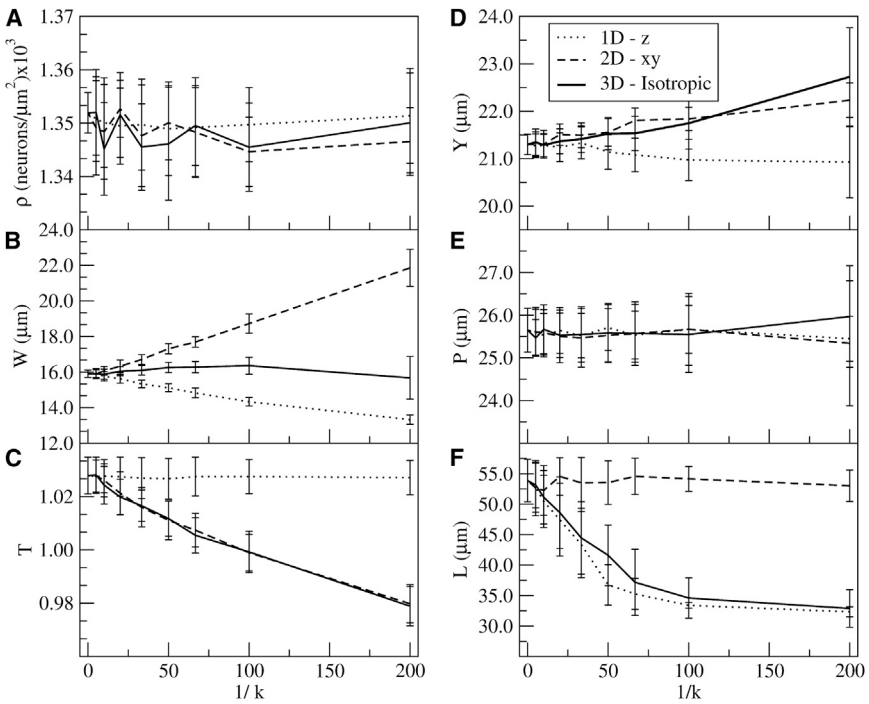

FIGURE 6 Microcolumnar measurements of neuronal systems undergoing different harmonic-force neuronal displacement mechanisms as a function of $1/k$. The graphs correspond to neuronal density, ρ (*A*), width, W (*B*), degree of microcolumnar periodicity, T (*C*), interneuronal distance of microcolumns, Y (*D*), intercolumn distance, P (*E*), and length, L (*F*).

In this article, we studied two dynamical models to elucidate the observed age-induced changes in microcolumnar organization in the rhesus monkey brain (46,47). We posit that the microcolumnar organization can be disrupted either by neuronal loss or by neuronal displacements where the total number of neurons is preserved. The two dynamical models tested thus consisted of deleting neurons and randomly displacing neurons in micrometer-size steps. The neuronal-deletion model consisted of two mechanisms: random deletions of single neurons and deletions of clusters of neurons. This model accounts for small but nonsignificant age-related decreases in neuronal density observed in experiments (42,44,53). In the neuronal-displacement model, three different mechanisms were tested: 1), displacements along the axis of the microcolumns (1D); 2), displacements in the plane perpendicular to the axis of the microcolumns (2D); and 3), displacements with no particular bias or direction (isotropic in 3D). Subtle neuronal displacements may occur in the cortex due to a degradation or loss of rigidity of the support matrix that keeps the somas in place (54–57). Each of the three displacement mechanisms would account for different plausible anatomical processes: loss of integrity in the apical dendrites and/or axons (1D), loss of support by the basal dendrites (2D), or general isotropic loss of support (3D). Our results indicate that in contrast to the deletion model, the harmonically restrained displacement model yields results consistent with measurements obtained experimentally for microcolumnarity in the aging rhesus monkey brain (46,47). All displacement mechanisms result in decay of microcolumnar strength when restorative forces are progressively weakened. Because the weakening of these restorative forces (increasing $1/k$) correlates with an increase in average neuronal displacements and thus increased spatial disorder, loss of rigidity and tissue coherence may be the mechanistic cause of loss of neuronal organization with age in the rhesus monkey brain.

On comparing the results of the different displacement mechanisms with experimental data, we observe that the 1D displacement model is not consistent with the observed effect of age on microcolumnar strength, suggesting that displacements along the axis of the microcolumn are less important than the other two degrees of freedom. This result is consistent with experimental data on the integrity of axons and apical dendrites, which, in comparison to the other anatomical structures that hold the soma in place, are not overly compromised with age (62). Experimental results indicate that the width of microcolumns is not affected by age (46), suggesting that the 3D isotropic model matches the observed behavior better than the 2D or 1D models. Because our models are idealized, it is possible that instead, a mixture of the mechanisms is present in vivo. For example, by modifying the 3D model with increased displacements in the perpendicular plane (that is, with k_z larger than but of the same order as k_x and k_y), the decrease in microcolumnar length could be lessened at the expense of some modest increase in microcolumnar width; thus, a mixture of the 2D and 3D mechanisms is possible. In general, our results suggest that the observed changes in microcolumnar properties with age are likely a destabilization of the matrix that holds the neuronal soma (apical and basal dendrites, axon, glia, and other supporting cells) in place.

The neuronal-deletion model tested whether small neuronal loss was consistent with experimental data. However, even considering a significant neuronal loss of 35%, the microcolumnar strength was unchanged by the uniform-deletion mechanism. This result follows from the definition of our measure for microcolumnar strength, which is the ratio of the density of neurons within a microcolumn to the global density of neurons. The cluster-deletion mechanism was inspired in part by previous work on spatial correlation of neuronal loss with amyloid deposits in transgenic mice models of Alzheimer's disease (63). Although it was not directly applicable to the mouse brain, since microcolumnarity was mainly observed in primates and humans, it may be applicable to neuropathological diseases associated with local neuronal loss.

Other works in the literature investigate microcolumnar properties in terms of neurological diseases and aging (49–52,64). In particular, microcolumnar thinning was demonstrated in human aging (50), suggesting microanatomical changes to neuronal circuitry that could be important in age and/or disease (50). The definition by Chance et al. (50) of thinning as the width of the microcolumn added to the two halves of the intercolumnar distances on each side is equivalent to our measure P, the intercolumnar distance. However, the quantity P was not found to significantly correlate with age in brains of rhesus monkeys. In our models, P is not affected, given the nature of their construction, our computational models did not consider changes in the intercolumn distances. Changes in P could be easily implemented, however, and, as an interesting follow-up to the modeling work presented here, could take into account changes in intermicrocolumnar distances using models of tissue shrinkage.

CONCLUSIONS

Here, we examined a 3D computational model to elucidate the observed changes in microcolumnar organization of neurons with age in rhesus monkey brains. A model that considers micrometer-size displacements of the spatial neuronal locations as a function of age is consistent with experimentally found microcolumnar measures. The model presented provides insights into age-related changes in the supporting matrix of neurons.

SUPPORTING MATERIAL

Twelve figures and Appendix A are available at http://www.biophysj.org/biophysj/supplemental/S0006-3495(14)00395-6.

We thank Dr. Robert Gilmore, Dr. Sam Kennerly, and Allyson O'Brien for discussions that strengthened the theory of this article and we acknowledge the National Science Foundation for allowing us access to the Extreme Science and Engineering Discovery Environment (XSEDE) supercomputing facilities through grant TG-PHYS100030 (B.U.). In addition, we thank Evelyn Henderson and Ashley Landicho for help editing and further strengthening our article.

We acknowledge funding provided by National Institutes of Health grant AG021133.

REFERENCES

1. Mountcastle, V. B. 1957. Modality and topographic properties of single neurons of cat's somatic sensory cortex. *J. Neurophysiol.* 20:408–434.
2. Mountcastle, V. B. 1997. The columnar organization of the neocortex. *Brain.* 120:701–722.
3. Buxhoeveden, D. P., and M. F. Casanova. 2002. The minicolumn hypothesis in neuroscience. *Brain.* 125:935–951.
4. Buxhoeveden, D. P., and M. F. Casanova. 2002. The minicolumn and evolution of the brain. *Brain Behav. Evol.* 60:125–151.
5. Constantinidis, C., M. N. Franowicz, and P. S. Goldman-Rakic. 2001. Coding specificity in cortical microcircuits: a multiple-electrode analysis of primate prefrontal cortex. *J. Neurosci.* 21:3646–3655.
6. DeFelipe, J., S. H. C. Hendry, …, E. G. Jones. 1990. A microcolumnar structure of monkey cerebral cortex revealed by immunocytochemical studies of double bouquet cell axons. *Neuroscience.* 37:655–673.
7. Mountcastle, V. B. 2003. Introduction. Computation in cortical columns. *Cereb. Cortex.* 13:2–4.
8. Peters, A., and C. Sethares. 1991. Organization of pyramidal neurons in area 17 of monkey visual cortex. *J. Comp. Neurol.* 306:1–23.
9. Peters, A., and C. Sethares. 1996. Myelinated axons and the pyramidal cell modules in monkey primary visual cortex. *J. Comp. Neurol.* 365:232–255.
10. Vercelli, A. E., D. Garbossa, …, G. M. Innocenti. 2004. Somatodendritic minicolumns of output neurons in the rat visual cortex. *Eur. J. Neurosci.* 20:495–502.
11. Casanova, M. F., J. Trippe, 2nd, …, A. E. Switala. 2010. Dolphin insula reflects minicolumnar organization of mammalian isocortex. *Transl Neurosci.* 1:37–42.
12. Ichinohe, N. 2012. Small-scale module of the rat granular retrosplenial cortex: an example of the minicolumn-like structure of the cerebral cortex. *Front. Neuroanat.* 5:69.
13. Peters, A., and D. A. Kara. 1987. The neuronal composition of area 17 of rat visual cortex. IV. The organization of pyramidal cells. *J. Comp. Neurol.* 260:573–590.
14. Buxhoeveden, D., and M. F. Casanova. 2005. Encephalization, minicolumns, and hominid evolution. *In* Neocortical Modularity and the Cell Minicolumn Nova Science, New York, pp. 117–136.
15. Jones, E. G. 2000. Microcolumns in the cerebral cortex. *Proc. Natl. Acad. Sci. USA.* 97:5019–5021.
16. Purves, D., D. R. Riddle, and A. S. LaMantia. 1992. Iterated patterns of brain circuitry (or how the cortex gets its spots). *Trends Neurosci.* 15:362–368.
17. Rockland, K. S., and N. Ichinohe. 2004. Some thoughts on cortical minicolumns. *Exp. Brain Res.* 158:265–277.
18. Swindale, N. V. 1990. Is the cerebral cortex modular? *Trends Neurosci.* 13:487–492.
19. Helmstaedter, M., C. P. J. de Kock, …, B. Sakmann. 2007. Reconstruction of an average cortical column in silico. *Brain Res. Brain Res. Rev.* 55:193–203.
20. Horton, J. C., and D. L. Adams. 2005. The cortical column: a structure without a function. *Philos. Trans. R. Soc. Lond. B Biol. Sci.* 360:837–862.
21. Krieger, P., T. Kuner, and B. Sakmann. 2007. Synaptic connections between layer 5B pyramidal neurons in mouse somatosensory cortex are independent of apical dendrite bundling. *J. Neurosci.* 27:11473–11482.
22. Opris, I., J. L. Fuqua, …, S. A. Deadwyler. 2012. Closing the loop in primate prefrontal cortex: inter-laminar processing. *Front. Neural Circuits.* 6:88.
23. Buldyrev, S. V., L. Cruz, …, B. T. Hyman. 2000. Description of microcolumnar ensembles in association cortex and their disruption in Alzheimer and Lewy body dementias. *Proc. Natl. Acad. Sci. USA.* 97:5039–5043.
24. Van Hoesen, G. W., and A. Solodkin. 1993. Some modular features of temporal cortex in humans as revealed by pathological changes in Alzheimer's disease. *Cereb. Cortex.* 3:465–475.
25. Benes, F. M., and E. D. Bird. 1987. An analysis of the arrangement of neurons in the cingulate cortex of schizophrenic patients. *Arch. Gen. Psychiatry.* 44:608–616.
26. Buxhoeveden, D., E. Roy, …, M. F. Casanova. 2000. Reduced interneuronal space in schizophrenia. *Biol. Psychiatry.* 47:681–683.
27. Casanova, M. F. 2009. Schizophrenia as a neurological condition caused by a failure in the lateralisation of the brain: macro and microscopic observations. *Rev. Neurol.* 49:136–142.
28. Casanova, M. F., P. Kreczmanski, …, C. Schmitz. 2008. Neuronal distribution in the neocortex of schizophrenic patients. *Psychiatry Res.* 158:267–277.
29. Di Rosa, E., T. J. Crow, …, S. A. Chance. 2009. Reduced neuron density, enlarged minicolumn spacing and altered ageing effects in fusiform cortex in schizophrenia. *Psychiatry Res.* 166:102–115.
30. Buxhoeveden, D., A. Fobbs, …, M. F. Casanova. 2002. Quantitative comparison of radial cell columns in children with Down's syndrome and controls. *J. Intellect. Disabil. Res.* 46:76–81.
31. Buxhoeveden, D. P., K. Semendeferi, …, E. Courchesne. 2007. Reduced minicolumns in the frontal cortex of patients with autism. *Neuropathol. Appl. Neurobiol.* 32:483–491. (Errata in *Neuropathol. Appl. Neurobiol.* 33:597; 33:720–721.)
32. Casanova, M. F. 2006. Neuropathological and genetic findings in autism: the significance of a putative minicolumnopathy. *Neuroscientist.* 12:435–441.
33. Casanova, M. F. 2008. The minicolumnopathy of autism: a link between migraine and gastrointestinal symptoms. *Med. Hypotheses.* 70:73–80.
34. Casanova, M. F., A. El-Baz, …, A. Farag. 2009. Reduced gyral window and corpus callosum size in autism: possible macroscopic correlates of a minicolumnopathy. *J. Autism Dev. Disord.* 39:751–764.
35. Casanova, M. F., A. El-Baz, …, A. Switala. 2010. A topographic study of minicolumnar core width by lamina comparison between autistic subjects and controls: possible minicolumnar disruption due to an anatomical element in-common to multiple laminae. *Brain Pathol.* 20:451–458.
36. Casanova, M. F., A. E. Switala, …, M. Fitzgerald. 2007. Comparative minicolumnar morphometry of three distinguished scientists. *Autism.* 11:557–569.
37. Casanova, M. F., I. van Kooten, …, C. Schmitz. 2006. Abnormalities of cortical minicolumnar organization in the prefrontal lobes of autistic patients. *Clin. Neurosci. Res.* 6:127–133.
38. Casanova, M. F., I. van Kooten, …, C. Schmitz. 2006. Minicolumnar width abnormalities in autism. *Biol. Psychiatry.* 59: 19S–19S.
39. Casanova, M. F., I. A. J. van Kooten, …, C. Schmitz. 2006. Minicolumnar abnormalities in autism. *Acta Neuropathol.* 112:287–303.
40. Williams, E. L., and M. F. Casanova. 2010. Autism and dyslexia: a spectrum of cognitive styles as defined by minicolumnar morphometry. *Med. Hypotheses.* 74:59–62.
41. Casanova, M. F., D. P. Buxhoeveden, …, E. L. Roy. 2002. Minicolumnar pathology in dyslexia. *Ann. Neurol.* 52:108–110.

42. Pakkenberg, B., and H. J. G. Gundersen. 1997. Neocortical neuron number in humans: effect of sex and age. *J. Comp. Neurol.* 384:312–320.

43. Pakkenberg, B., D. Pelvig, …, L. Regeur. 2003. Aging and the human neocortex. *Exp. Gerontol.* 38:95–99.

44. Peters, A., J. H. Morrison, …, B. T. Hyman. 1998. Feature article: are neurons lost from the primate cerebral cortex during normal aging? *Cereb. Cortex.* 8:295–300.

45. Cruz, L., S. V. Buldyrev, …, D. L. Rosene. 2005. A statistically based density map method for identification and quantification of regional differences in microcolumnarity in the monkey brain. *J. Neurosci. Methods.* 141:321–332.

46. Cruz, L., D. L. Roe, …, D. L. Rosene. 2004. Age-related reduction in microcolumnar structure in area 46 of the rhesus monkey correlates with behavioral decline. *Proc. Natl. Acad. Sci. USA.* 101:15846–15851.

47. Cruz, L., D. L. Roe, …, D. L. Rosene. 2009. Age-related reduction in microcolumnar structure correlates with cognitive decline in ventral but not dorsal area 46 of the rhesus monkey. *Neuroscience.* 158:1509–1520.

48. Cruz, L., B. Urbanc, …, H. E. Stanley. 2008. Generating a model of the three-dimensional spatial distribution of neurons using density maps. *Neuroimage.* 40:1105–1115.

49. Chance, S. A., M. F. Casanova, …, M. M. Esiri. 2006. Minicolumn thinning in temporal lobe association cortex but not primary auditory cortex in normal human ageing. *Acta Neuropathol.* 111:459–464.

50. Chance, S. A., L. Clover, …, M. M. Esiri. 2011. Microanatomical correlates of cognitive ability and decline: normal ageing, MCI, and Alzheimer's disease. *Cereb. Cortex.* 21:1870–1878.

51. van Veluw, S. J., E. K. Sawyer, …, S. A. Chance. 2012. Prefrontal cortex cytoarchitecture in normal aging and Alzheimer's disease: a relationship with IQ. *Brain Struct. Funct.* 217:797–808.

52. Peters, A., and T. Kemper. 2012. A review of the structural alterations in the cerebral hemispheres of the aging rhesus monkey. *Neurobiol. Aging.* 33:2357–2372.

53. Morrison, J. H., and P. R. Hof. 1997. Life and death of neurons in the aging brain. *Science.* 278:412–419.

54. Jäger, C., D. Lendvai, …, M. Morawski. 2013. Perineuronal and perisynaptic extracellular matrix in the human spinal cord. *Neuroscience.* 238:168–184.

55. Morawski, M., G. Brückner, …, R. T. Matthews. 2012. Aggrecan: beyond cartilage and into the brain. *Int. J. Biochem. Cell Biol.* 44:690–693.

56. Morawski, M., M. K. Brückner, …, T. Arendt. 2004. Perineuronal nets potentially protect against oxidative stress. *Exp. Neurol.* 188:309–315.

57. Wu, Y., J. Wu, …, B. B. Yang. 2005. Versican protects cells from oxidative stress-induced apoptosis. *Matrix Biol.* 24:3–13.

58. West, M. J., P. D. Coleman, …, J. C. Troncoso. 1994. Differences in the pattern of hippocampal neuronal loss in normal ageing and Alzheimer's disease. *Lancet.* 344:769–772.

59. Arendt, T., V. Bigl, …, A. Tennstedt. 1983. Loss of neurons in the nucleus basalis of Meynert in Alzheimer's disease, paralysis agitans and Korsakoff's Disease. *Acta Neuropathol.* 61:101–108.

60. Gómez-Isla, T., R. Hollister, …, B. T. Hyman. 1997. Neuronal loss correlates with but exceeds neurofibrillary tangles in Alzheimer's disease. *Ann. Neurol.* 41:17–24.

61. Chance, S. A., E. K. Sawyer, …, T. J. Crow. 2013. Hemispheric asymmetry in the fusiform gyrus distinguishes *Homo sapiens* from chimpanzees. *Brain Struct. Funct.* 218:1391–1405.

62. Peters, A., D. L. Rosene, …, M. S. Albert. 1996. Neurobiological bases of age-related cognitive decline in the rhesus monkey. *J. Neuropathol. Exp. Neurol.* 55:861–874.

63. Urbanc, B., L. Cruz, …, B. T. Hyman. 2002. Neurotoxic effects of thioflavin S-positive amyloid deposits in transgenic mice and Alzheimer's disease. *Proc. Natl. Acad. Sci. USA.* 99:13990–13995.

64. Casanova, M. F., A. El-Baz, and A. Switala. 2011. Laws of conservation as related to brain growth, aging, and evolution: symmetry of the minicolumn. *Front. Neuroanat.* 5:66.